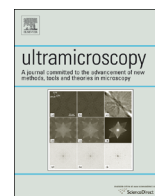




ELSEVIER

Contents lists available at ScienceDirect

Ultramicroscopy

journal homepage: www.elsevier.com/locate/ultramic

When to use the projection assumption and the weak-phase object approximation in phase contrast cryo-EM



Miloš Vulović^{a,b,1}, Lenard M. Voortman^{a,1}, Lucas J. van Vliet^a, Bernd Rieger^{a,*}

^a Quantitative Imaging Group, Faculty of Applied Sciences, Delft University of Technology, Lorentzweg 1, 2628 CJ Delft, The Netherlands

^b Electron Microscopy Section, Molecular Cell Biology, Leiden University Medical Center, P.O. Box 9600, 2300 RC Leiden, The Netherlands

ARTICLE INFO

Article history:

Received 11 March 2013

Received in revised form

31 July 2013

Accepted 8 August 2013

Available online 17 August 2013

Keywords:

Cryo-electron microscopy

Exit waves

Image simulation

Thick-phase grating

Interaction potential

ABSTRACT

The projection assumption (PA) and the weak-phase object approximation (WPOA) are commonly used to model image formation in cryo-electron microscopy. For simulating the next step in resolution improvement we show that it is important to revisit these two approximations as well as their limitations. Here we start off by inspecting both approximations separately to derive their respective conditions of applicability. The thick-phase grating approximation (TPGA) imposes less strict conditions on the interaction potential than PA or WPOA and gives comparable exit waves as a multislice calculation. We suggest the ranges of applicability for four models (PA, PA+WPOA, WPOA, and TPGA) given different interaction potentials using exit wave simulations. The conditions of applicability for the models are based on two measures, a worst-case (safest) and an average criterion. This allows us to present a practical guideline for when to use each image formation model depending on the spatial frequency, thickness and strength of the interaction potential of a macromolecular complex.

© 2013 Elsevier B.V. All rights reserved.

1. Introduction

Quantitative forward modeling of image formation and the simulation of images are becoming increasingly important in order to optimize the data acquisition strategy, facilitate reconstruction schemes, improve image interpretation and resolution, and provide insight into ways to improve instrumentation. An accurate description of the interaction between incident electrons and the specimen is one of the important steps in forward modeling, contrast transfer function (CTF) correction and 3D reconstruction in cryo-electron microscopy (cryo-EM).

In cryo-EM, incident electrons with typical energies of 80–300 keV interact with the electrostatic interaction potential (IP) of the specimen, e.g. macromolecules that are similar in density to the surrounding vitreous ice. In order to describe the electron–specimen interaction (analytically) two approximations are often made: the weak-phase object approximation (WPOA) and the projection assumption (PA). The WPOA holds for weakly scattering objects [1] and the PA assumes that the exit wave from the specimen can be computed via the projected IP of the whole specimen [2]. Both approximations rely on the small angle approximation [3] and are frequently used at the same time.

Applying both approximations greatly simplifies the computational complexity of forward modeling and 3D reconstruction and therefore they have been implemented in most software packages for single particle analysis (SPA) and electron tomography (ET) [4–9].

These approximations have, of course, limitations as they cannot account for e.g. the curvature of the Ewald sphere or multiple scattering events [10]; effects which become more critical for high resolution imaging. In materials science high resolution electron microscopy (HREM), where atomic resolution is attained on certain specimens, a multislice calculation [2] is commonly used to overcome the limitations of the aforementioned approximations in modeling the transmission of the electron wave through the specimen. There, the specimen is divided into slices and propagation of the electron wave can be interpreted as a successive transmission and propagation through each slice until the wave leaves the specimen. The PA must hold within each slice and therefore, it is also important to formulate a quantitative criterion to determine the appropriate slice thickness. The multislice approach has been rarely used in cryo-EM [11,12] mainly because of the lower resolution of cryo-EM compared to HREM. Due to the need for higher resolution in cryo-EM, it is important to revisit the WPOA and PA and investigate their applicabilities.

The thick-phase grating approximation (TPGA) was introduced in HREM of perfect crystals in 1962 [13,14], but to the best of our knowledge, it has not received much attention since. They provided rough indications for the validity of various approximations

* Corresponding author. Tel.: +31 15 2788574.

E-mail address: b.rieger@tudelft.nl (B. Rieger).

¹ These authors contributed equally to this work.

depending on the thickness and atomic number of the crystals. In [15], the multislice (MS) method was used to discuss the breakdown of the PA in HREM of amorphous samples and the consequence of the breakdown on the measurement of microscope parameters, especially spherical aberration. In [16] the ranges of validity for the WPOA for organic crystals are discussed in terms of thickness, resolution and incident electron energy. Although they use a quantitative measure (dissimilarity factor [17]), only single scattering approximations were considered.

Here, we introduce TPGA to the field of cryo-EM and discuss its potential benefits. We provide practical boundaries to various approximations based on the thickness, strength and frequency of the interaction potential map.

2. High-energy electron and specimen interaction

To discuss the validity of the PA and WPOA it is convenient to start from the stationary one-body Schrödinger equation with a correction for the relativistic mass and wavelength of the electron (see e.g. [18]). This is permitted for elastic scattering processes as inter alia (i) the Hamiltonians of the electron and the specimen can be separated because the incident electrons have a much higher energy than the interaction energy of the particles within the specimen, (ii) spin–spin interactions may be neglected, and (iii) the electron current in cryo-EM is low so that effectively only one electron interacts with the specimen at the same time, which guarantees independence of all incident electrons. Below we will shortly recapitulate the formulae commonly used in HREM [14,2].

2.1. Small angle approximation

The stationary one-body Schrödinger equation for the electron wave function in a closed system is given by

$$\left(-\frac{\hbar^2}{2m}\nabla_{\mathbf{r}}^2 + e\mathcal{V}(\mathbf{r})\right)\psi_e(\mathbf{r}) = E_e\psi_e(\mathbf{r}), \quad (1)$$

where $-\hbar^2/(2m)\nabla_{\mathbf{r}}^2$ is the Hamiltonian of the incident high-energy electron, which in this case represents its kinetic energy, $\mathcal{V}(\mathbf{r})$ the interaction potential, \hbar the reduced Planck constant, m the relativistic mass of the electron, e the electron charge, $\mathbf{r} = (x, y, z) = (\boldsymbol{\rho}, z)$ the position, ψ_e the electron wave function, and E_e the energy of the incident electron.

The incident electron travels (spirals) predominately along the optical axis, i.e. the z -direction. The specimen constitutes a relatively small perturbation to this motion. Therefore the total electron wave function $\psi_e(\mathbf{r})$ can be written as a product of a plane wave traveling in the z -direction and a wave function Ψ which varies slowly with z , i.e. $\psi_e(\mathbf{r}) = \Psi(\mathbf{r})e^{ikz}$, with the wave vector $k = 2\pi/\lambda = \sqrt{2mE_e}/\hbar$, and λ being the wavelength. Now it follows from Eq. (1)

$$\left(\nabla_{\boldsymbol{\rho}}^2 + \partial_z^2 + 2ik\partial_z - \frac{2me}{\hbar^2}\mathcal{V}(\mathbf{r})\right)\Psi(\mathbf{r}) = 0. \quad (2)$$

Given the assumptions that the energy of the incident electron is high and that Ψ varies slowly with z , it holds that $|\partial_z^2\Psi| \ll |k\partial_z\Psi|$ and $k^2 \gg k_x^2 + k_y^2$, which is known as the small angle approximation. With the definition of the interaction constant $\sigma = \lambda me/(2\pi\hbar^2)$, this leads to

$$\partial_z\Psi(\mathbf{r}) = \left(\frac{i\lambda}{4\pi}\nabla_{\boldsymbol{\rho}}^2 + i\sigma\mathcal{V}(\mathbf{r})\right)\Psi(\mathbf{r}). \quad (3)$$

Taking the 2D Fourier-transform in $\boldsymbol{\rho} = (x, y)$ we get our common starting point for all further approximations

$$\partial_z\mathcal{F}_{\boldsymbol{\rho}}[\Psi] = -i\lambda\pi q^2\mathcal{F}_{\boldsymbol{\rho}}[\Psi] + i\sigma\mathcal{F}_{\boldsymbol{\rho}}[\mathcal{V}\Psi], \quad (4)$$

in which the Fourier-transform is defined as $\mathcal{F}_{\boldsymbol{\rho}}[f(\boldsymbol{\rho})](\mathbf{q}) = \iint f(\boldsymbol{\rho})e^{-2\pi i\boldsymbol{\rho}\mathbf{q}} d\boldsymbol{\rho}$.

3. Bounds to projection assumption and weak-phase object approximation

To solve Eq. (4) analytically, further simplifications are needed. Two common approximations in cryo-EM are the projection assumption (PA) and the weak-phase object approximation (WPOA), where the latter is also known as kinematic approximation [19]. These two approximations lead to four different models describing the electron–specimen interaction. Below we will provide rules-of-thumb when to use each of these models.

Without loss of generality it is assumed that before the wave function Ψ is scattered by the potential \mathcal{V} it has a constant magnitude and zero phase. The magnitude of the incident wave is conveniently set to 1. The scattered part of the wave function Ψ_{sc} is then given by $\Psi = 1 + \Psi_{sc}$.

Contrast in cryo-EM is formed predominately by phase contrast [10]. Because scattering by a constant \mathcal{V}_0 is identical to rescaling the wavelength, i.e. adding a constant phase factor to the incident electron wave, elastic scattering from the mean bulk potential does not contribute to contrast generation. Since we are interested in that part of the scattering process that produces contrast, we subtract the mean bulk potential. This is known as the quasi-kinematic approximation [19].

3.1. Projection assumption

When the specimen is sufficiently thin, the projection assumption (PA) is commonly used [2]. Then the propagation term of Eq. (3) is small compared to the interaction term, i.e. $|(i\lambda/4\pi)\nabla_{\boldsymbol{\rho}}^2\Psi| \ll |i\sigma\mathcal{V}\Psi|$. From Eq. (3) it follows

$$\partial_z\Psi(\mathbf{r}) = i\sigma\mathcal{V}(\mathbf{r})\Psi(\mathbf{r}) \Rightarrow \Psi = \exp\left\{i\sigma\int_{-\infty}^z \mathcal{V} dz'\right\}, \quad (5)$$

which leads to the exit wave

$$\Psi_{\text{exit}} = \exp\{i\sigma\mathcal{V}_z\}, \quad (6)$$

with the projected potential $\mathcal{V}_z = \int_{-\infty}^{\infty} \mathcal{V} dz$. The validity of the PA was addressed by [20]. They argue that the potential should not vary significantly over a distance $d_r \geq \sqrt{\lambda\Delta z}/(2\pi)$, where Δz is the thickness of the specimen. Here, we will define a quantitative criterion for the validity of the assumption based on the Fresnel number. We define it in analogy to optics as $F = \Delta r^2/(\lambda\Delta z)$ [21], where Δr is the voxel size of the discretized potential map. Note that the regime $F \gg 1$ corresponds to ray optics and $F \geq 1$ to the small angle approximation. If we assume the Nyquist sampling of the potential map, we have $q < 1/(2\Delta r)$ and the spatial frequencies up to which the projection assumption holds, which is given by

$$q \ll \sqrt{1/(4\lambda\Delta z)}. \quad (7)$$

In the above considerations there is no requirement for weak scattering. In this case, the absolute value of the potential is not relevant and the PA can also be valid for a strong-phase object. Note that the PA is also known as *phase-object approximation* or *phase-grating approximation* [14,3].

3.2. Projection assumption and weak-phase object approximation

If the scattering is weak, which is the case for most atoms in biological samples, the weak-phase object approximation (WPOA) $\sigma\mathcal{V}_z < 1$ can be used. When both PA and WPOA hold, Eq. (6) can be

approximated by

$$\Psi_{\text{exit}} = 1 + i\sigma\mathcal{V}_z + \mathcal{O}(\sigma^2\mathcal{V}_z^2). \quad (8)$$

Since $\sigma\mathcal{V}_z < 1$ leads to a scattered wave $\Psi_{\text{sc}} < 1$, the above result can also be obtained by substituting $\Psi = 1$ into the rhs of Eq. (5) giving $\partial_z\Psi = i\sigma\mathcal{V}$. We will refer to Eq. (8) as PA+WPOA.

3.3. Weak-phase object approximation

The applicability of the WPOA depends on how well $\exp(i\sigma\mathcal{V}_z)$ can be approximated by a first order Taylor series expansion with $\mu = \sigma\mathcal{V}_z$,

$$e^{i\mu} = 1 + i\mu + \mathcal{O}(\mu^2). \quad (9)$$

The relative residual in orders m or higher is given by

$$p(m, \mu) = e^{-\mu} \sum_{n=m}^{\infty} \frac{\mu^n}{n!}, \quad (10)$$

where $e^{-\mu}$ normalizes the total sum $p(0, \mu)$ to 1. If we allow for a maximum of e.g. 5% in second and higher order terms, we solve $p(2, \sigma\mathcal{V}) = 0.05$ to find

$$\sigma\mathcal{V}_z < 0.36. \quad (11)$$

We will use this condition for applying the WPOA.

Note that Eq. (10) is identical to the probability of multiple scattering events described by a Poisson distribution with scattering probability $\mu = d/\Lambda$, in which d is the path length and Λ the mean free path [22]. This allows the interpretation of the different orders $\mathcal{O}(\sigma\mathcal{V}_z)$ as scattering events.

In a typical cryo-EM experiment, the macromolecular complex is embedded in vitreous ice whose thickness is larger than the thickness of the macromolecular complex. If we assume that vitreous ice is characterized by a bulk mean potential $\mathcal{V}_{\text{ice}} > 0$, the process of multiple scattering by a constant \mathcal{V}_{ice} can be neglected in the quasi-kinematic approach. Therefore, the condition given by Eq. (11) can only be applied to the mean-subtracted projected potential.

When the resolution of the potential map is too high to allow satisfying the PA condition, we can still use the WPOA. Furthermore, using only the WPOA results in an easy to implement algorithm for forward modeling. With the assumption $\sigma\mathcal{V}_z < 1$ or equally $\Psi_{\text{sc}} < 1$, Eq. (4) can be solved as follows:

$$\begin{aligned} \partial_z \mathcal{F}_\rho[\Psi] &= -i\lambda\pi q^2 \mathcal{F}_\rho[\Psi] + i\sigma \mathcal{F}_\rho[\mathcal{V}] \\ \Rightarrow \mathcal{F}_\rho[\Psi] &= 1 + i\sigma \int_{-\infty}^z e^{-i\lambda\pi q^2 z'} \mathcal{F}_\rho[\mathcal{V}] dz' \\ \mathcal{F}_\rho[\Psi_{\text{exit}}] &= 1 + i\sigma \int \mathcal{V}(\rho, z) e^{-2\pi i(\rho\mathbf{q} + (1/2)\lambda q^2 z)} d\mathbf{r} \\ \Psi_{\text{exit}} &= 1 + i\sigma \mathcal{F}_\rho^{-1}[\mathcal{F}[\mathcal{V}](\mathbf{q}, \lambda q^2/2)], \end{aligned} \quad (12)$$

here $\mathcal{F}[\mathcal{V}]$ is the 3D Fourier transform of the potential evaluated at the coordinate $(\mathbf{q}, \lambda q^2/2)$, with $\mathbf{q} = (q_x, q_y)$. Computation of the 3D Fourier-transform sampled on the parabola $(\mathbf{q}, \lambda q^2/2)$ can be done accurately and fast, as in [23].

3.4. Thick-phase grating approximation

The limitations of the PA and WPOA can be overcome by the thick-phase grating approximation (TPGA) [13,14]. Initially developed for perfect crystals with respect to both diffraction and imaging, the TPGA applied to cryo-EM represents the fourth combination resulting from the PA and WPOA and gives the following forward model:

$$\Psi_{\text{exit}} = \exp\{i\sigma \mathcal{F}_\rho^{-1}[\mathcal{F}[\mathcal{V}](\mathbf{q}, \lambda q^2/2)]\}. \quad (13)$$

The advantage of this combination is that in the limit of $F \gg 1$, Eq. (13) converges to Eq. (6) and in the limit of $\sigma\mathcal{V} \ll 1$, Eq. (13)

converges to Eq. (12). This means that we get the corresponding image models of PA or WPOA directly from the above equation in their respective limits.

The approximations of Eqs. (6), (8) and (12) were derived in a similar way in [3]. Quantitative useful conditions for the validity of the approximations of Eqs. (11) and (7) are presented here. Their advantages will be demonstrated below.

4. Results

4.1. Hemoglobin

Here we investigate the validity of the PA and WPOA for *Lumbricus terrestris erythrocrucorin* (earth worm hemoglobin – PDBid 2GTL) interacting with 80 keV electrons. This is a representative sample in terms of scattering power and size in cryo-EM. The interaction potential (IP) is computed as the sum of isolated atomic potentials. The atomic potential is calculated as the Fourier transform of the electron scattering factor which is parameterized as a weighted sum of five Gaussians [24]. All samples in this analysis are embedded in vitreous ice ($\rho = 0.93 \text{ g/cm}^3$) which was modeled as a continuous medium. A detailed description of how the IP is constructed can be found elsewhere [12].

Fig. 1 shows the validity of both approximations for this sample as a function of spatial frequency for various slice thicknesses. The graph shows the maximum value of the projected IP for a given slice thickness that we computationally extracted from the middle of the full IP. By doing so we can simulate the influence of the sample thickness and hereby indirectly the influence of the potential strength on the validity of the assumptions. The thickness of the slices was varied from 2.0 to 32.5 nm, eventually containing the entire specimen.

The values on the $\sigma\mathcal{V}_z$ -axis are calculated using the maximum projected potential of a slice extracted from the middle of the full map. We show one line for a potential map sampled at 1 Å (green) and one at 3 Å (blue) which are given by Eq. (7), i.e. the Fresnel

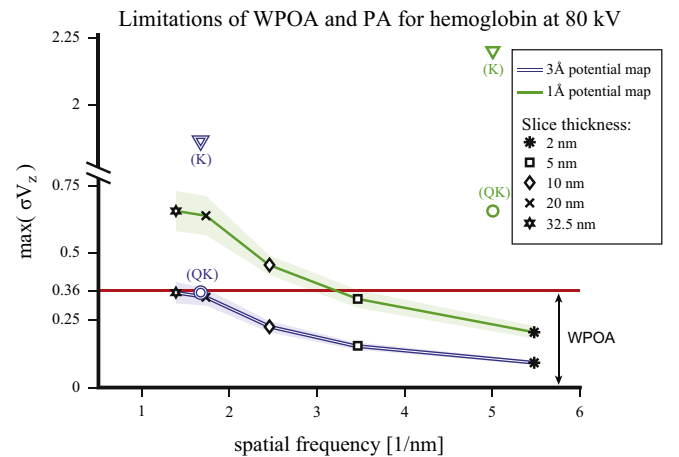


Fig. 1. Validity of the PA and WPOA for hemoglobin interacting with 80 keV electrons for various slice thicknesses. The green and blue lines depict the boundary given by the Fresnel number $F=1$ (compare Eq. (7)) for a potential map sampled at 1 Å and 3 Å respectively as a function of slice thickness. For each thickness, one slice is computationally extracted from the middle of the full IP (not to be confused with the multislice method). The shaded area around the lines denotes the variation due to possible slice orientations. The WPOA is valid below the red line, $\sigma\mathcal{V}_z < 0.36$, while the PA starts to hold for regions left/below to the blue or green line depending on the sampling of the map. The circles indicate the full map of hemoglobin at the respective sampling in the quasi-kinematic (QK) approach, whereas the triangles show the kinematic approach (K). (For interpretation of the references to color in this figure caption, the reader is referred to the web version of this article.)

number is equal to one. The uncertainty of the plotted values due to specimen orientation is depicted by the shaded area around the lines. Left/below of the respective lines the PA starts becoming suitable, whereas right/above it is violated. As given by Eq. (11), below the horizontal line $\sigma\mathcal{V}_z = 0.36$ the WPOA holds. For the full potential map sampled at 1 Å (green circle), neither PA nor WPOA holds, whereas for the potential map sampled at 3 Å (blue circle) the WPOA is satisfied and the PA is found to be right at the border. We see from Fig. 1 that the criteria for WPOA and PA are easier fulfilled for low-frequency potential maps (e.g. when the potential is blurred by beam-induced movements, CTF and/or the camera transfer). For a comparison we show in Fig. 1 the quasi-kinematic (QK) and the kinematic (K) potentials as circles and triangles, respectively. The kinematic potential represents the absolute strength of the potential, while the quasi-kinematic potential refers to the mean-subtracted potential relevant for the generated phase contrast. Here we used $\max(\sigma\mathcal{V}_z)$ as condition for the ranges of application for the different approximations, which gives a so-called worst-case (safest) condition.

4.2. Exit waves of a tubulin tetramer

For a tubulin tetramer (TT) constructed from PDBid –1SAO ($\Delta z = 27$ nm) we show in Fig. 2A the computed phase of the exit wave after interaction with 80 keV electrons using the four approximations discussed above, i.e. PA, PA+WPOA, WPOA and TPGA. The potential map was sampled at 1 Å. In order to better visualize the effect of the approximations, we show in Fig. 2B the differences of the four exit waves with a reference. This reference is computed by a multislice (MS) approach inspired by [2]. Since we use the MS method here only for computing the reference, the slice thickness is set equal to the resolution of the potential map. In the difference images of Fig. 2B we observe that the TPGA is nearly identical to the MS reference, whereas the WPOA shows deviations mostly in the stronger phase parts. For the PA we see deviations especially at the periphery of TT and, of course, for the combined PA+WPOA the deviations are the largest.

4.3. Synthetic amorphous test specimen

We simulate exit waves of a synthetic test specimen using Eqs. (6), (12), (8) and (13) to study the validity of the predicted limits for the cases PA and WPOA. For the cases PA+WPOA and TPGA we want to investigate where the limits of the validity of these combined approximations lie. Our derived conditions of Eqs. (7) and (11) are functions of the maximum spatial frequency, thickness and strength of the interaction potential. Therefore, a synthetic test potential must have these properties as well. The simplest potential that fulfills these criteria is a low-pass filtered Gaussian white-noise specimen of a specified thickness. This

synthetic specimen resembles an amorphous material such as a carbon film.

The criterion for the WPOA Eq. (11) depends on the strength of the interaction potential. But since we are only interested in the scattering that produces phase contrast, the mean bulk potential can be ignored (quasi-kinematic). As a consequence $\sigma\mathcal{V}_z$ is not well defined as $\langle\sigma\mathcal{V}_z\rangle = 0$. An alternative is to consider $\max(|\sigma\mathcal{V}_z|)$ as we did in Section 4.1. This measure, however, depends for the synthetic test specimen on its spatial extent in (x,y) . Therefore, we will examine the standard deviation $\text{std}(\sigma\mathcal{V}_z)$ for our synthetic test specimens. For potential maps of a macromolecule, $\text{std}(\sigma\mathcal{V}_z)$ depends on the size of the (vacuum) bounding box, in contrast to $\max(|\sigma\mathcal{V}_z|)$, which does not.

To test the applicability of the different approximations we again compare the four simulated exit waves against the MS reference. To quantify the difference between two exit waves we use the normalized mean squared error (MSE), where the standard deviation of the reference exit wave is used for normalization. This normalization is necessary to ensure a proper comparison of MSEs originating from exit waves with varying $\text{std}(\sigma\mathcal{V}_z)$. Fig. 3A shows the result of thresholding the MSE at 10%. We find a horizontal boundary for the WPOA and a vertical boundary for the PA, as expected from Eqs. (7) and (11). The combined models have boundaries which asymptotically approach the individual (WPOA and PA) approximations. In Fig. 3B a sketched version depicts the qualitative results in terms of regions where the different approximations hold.

In addition to the conditions that quantify the applicability for our synthetic specimen (Fig. 3), we want to make a reproducible classification of the approximations for actual three-dimensional potential maps of macromolecules based on their potential properties. Therefore, we need to estimate the potential properties such that a synthetic specimen with that specification behaves similar to the actual potential under the different approximations (i.e. results expressed in similar MSEs against a MS reference). In Fig. 3A we show the characteristics of three macromolecules (ribosomal subunit from *haloarcula marismortui* – PDBid –1FFK, earth worm hemoglobin and TT) sampled at 1 Å and 3 Å voxel sizes.

For the characteristic properties of each potential map we must calculate (i) the maximum spatial frequency, (ii) the thickness, and (iii) the strength of the interaction potential. These properties can be ambiguous for a macromolecular potential as e.g. the size of the bounding box of the complex influences $\text{std}(\sigma\mathcal{V}_z)$. As a solution we propose (i) to retrieve the maximum spatial frequency by finding the 65th percentile of the 2D power spectrum of \mathcal{V}_z , (ii) to obtain the thickness by first computing $\text{std}(\mathcal{V}(\rho, z))$ as a function of z , then finding the 2.5th and the 97.5th percentile (i.e. the top and bottom of the protein respectively), and (iii) to estimate the strength of the IP by masking any background from the map, then finding the 80th percentile of the histogram of $|\mathcal{V}_z - \langle\mathcal{V}_z\rangle|$. The corresponding

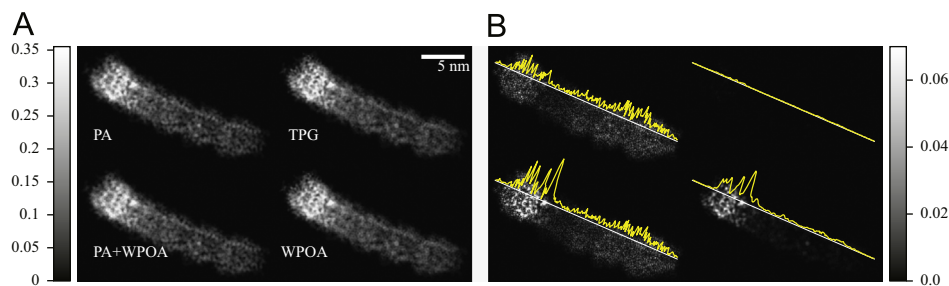


Fig. 2. (A) Simulated phases of exit waves of a tubulin tetramer (HT = 80 kV) using the PA via Eq. (6), WPOA via Eq. (12), PA+WPOA via Eq. (8) and TPGA via Eq. (13). (B) Difference image of the exit waves in (A) and the exit wave computed with a MS approach. Graph insets show the intensity along the line. The intensity scale bar indicates the phase of the exit wave subtracted by its mean.

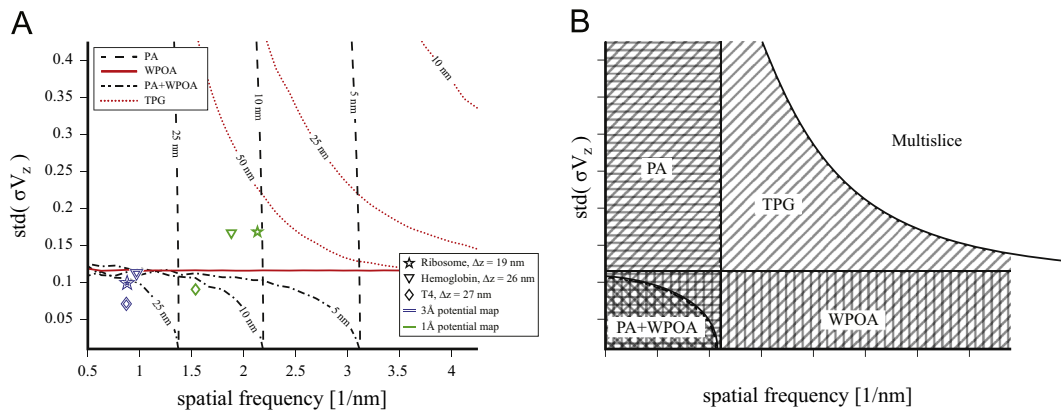


Fig. 3. The applicability (at $HT=80$ kV) of the PA, PA+WPOA, WPOA, and TPGA. (A) Boundaries for each approximation where different lines represent different specimen thicknesses. Lines indicate 10% MSE error of the respective approximations with a MS reference. Left/below the boundary the approximation holds for a particular thickness. Three protein-complex potentials map (ribosome, hemoglobin, TT) sampled at 1 Å and 3 Å are included (see main text for details). (B) A sketched diagram showing the qualitative results of (A). The various striped regions depict region where each approximation holds.

values for the three macromolecules are depicted in Fig. 3A (star, triangle and diamond). The specific values for each percentile were chosen such that a synthetic specimen with the estimated properties yields similar MSEs as the actual potential. The aim of the above procedure is to transfer the general conclusions from synthetic test specimens to actual macromolecular potentials. This procedure allows other macromolecules to be classified into regions based on the boundaries of applicability as depicted in Fig. 3A.

Now we see in Fig. 3 that the three proteins sampled at 3 Å satisfy both the PA and WPOA and are close to the PA+WPOA boundary. When sampled at 1 Å the PA is not satisfied and only TT satisfies the WPOA. The hemoglobin results agree with those shown in Fig. 1. Judging from Fig. 2, which shows TT, we could conclude that the WPOA is violated for some parts of the molecule. In Fig. 3, however, we see that on average TT satisfies the WPOA. This apparent contradiction is due to the fact that Fig. 3 is computed from the average measure $\text{std}(\sigma V_z)$, instead of $\max(|\sigma V_z|)$ in Fig. 1.

5. Discussion

In this paper we proposed quantitative criteria for the applicability of the PA (via the Fresnel number) and WPOA (via the probability of multiple interactions) in phase contrast cryo-EM. In [13] rough indications were provided for the validity of various forward approximations in HREM depending on the thickness and atomic number of the crystals. Depending on the magnitude of the error one considers acceptable, their boundaries (evaluated at one spatial frequency) are consistent with our criteria.

Here, in addition to the MS approach, the proposed criteria motivate the existence of four models describing the electron wave propagation through the specimen (PA, PA+WPOA, WPOA, and TPGA). The choice of the model depends on the strength, frequency content and thickness of the interaction potential map. Furthermore, the TPGA is applied here to realistic specimen models in the cryo-EM field.

The MS method is the most accurate of the aforementioned methods and was utilized as a reference. The reasons for the little usage of MS in cryo-EM [11,12] are related to the lower resolution of the structures studied by cryo-EM compared to HREM, and because it leads to a more complicated inverse problem in 3D reconstruction. Potential difficulties of the 3D reconstruction based on MS can be partially avoided by using a directly invertible approximation (e.g. WPOA or PA+WPOA) in the first iteration of a

typical iterative reconstruction scheme. As shown in Fig. 2, the simulations indicate that the direct TPGA approach gives nearly identical exit waves as a recursive MS calculation. We expect, however, that TPGA can be advantageous for 3D reconstructions due to its invertibility and the possibility to utilize the non-uniform fast Fourier transform in the sampling of the Ewald sphere [23,25].

For the sake of completeness it should be mentioned that in materials science the projected charge density approximation (PCDA) [14,26] is also used. The PCDA provides a linear expression between the intensity and projected charge density, but assumes that the CTF is parabolic. In cryo-EM, PCDA is usually violated owing to much higher defocus values compared to materials science. For example, at 300 kV and 1–2 μm defocus, the frequency up to which PCDA is satisfied (10% error) would be around 3–4 nm^{-1} . This is not sufficiently accurate for SPA; for tomography, a higher defocus needs to be employed limiting the validity of the PCDA to frequencies lower than 6–12 nm^{-1} .

The presented simulations of an amorphous test specimen serve as a practical reference to facilitate the model choice for electron wave propagation through an actual macromolecule such as hemoglobin, ribosome, or tubulin. The accuracy of each approximation depends on the properties of the potential under investigation. In order to describe the relevant potential properties we introduced two measures: $\max(|\sigma V_z|)$ and $\text{std}(\sigma V_z)$. The former represents the worst-case (safest) boundary and the latter an average boundary for which the approximations hold.

We deliberately present all our results for $HT=80$ kV because for higher HT (shorter wavelength), the approximations given by Eqs. (11) and (7) are relaxed as $\sigma \propto \lambda$. The criteria for WPOA and PA are also easier to satisfy for potential maps of lower resolution (compare Figs. 1 and 3). Note that we do not make claims about the resolution in the final recorded images as it depends for a large part on the electron count, beam-induced movements, CTF, and camera characteristics. It is, however, clear that the electron-specimen interaction model needs to be accurate up to spatial frequencies as least as high as the resolution of the final image.

Under typical circumstances inelastic scattering influences the total contrast and we do not record pure phase contrast. Nevertheless, the findings in this paper are important since phase contrast is the primary contrast mechanism in cryo-EM [1]. In our analysis the mean value of the IP was subtracted (quasi-kinematic approach) since it does not contribute to the phase contrast. For inelastic scattering, modeled as the imaginary part of the IP [19], the mean potential cannot be neglected since it damps the magnitude of the exit wave. Here, only the relative difference

between exit waves is analyzed. Therefore, damping due to the mean imaginary potential does not influence our findings. Nevertheless, the contrast in the final images does depend on inelastic scattering which requires a deeper investigation.

Although amorphousness of the vitreous ice would be apparent in the simulated images of the exit waves, we modeled the ice as a constant background. In [12] it has been shown that for typical electron fluxes in cryo-EM ($< 100e^-/A$), the influence of the solvent amorphousness in the final images can be neglected. Any averaging technique to enhance the SNR would blur out the structural noise.

As practical conclusions we find that when simulating images at resolutions of ~ 5 Å, the applicability of the PA and WPOA needs to be re-considered. Here, the TPGA offers an excellent solution, as an alternative to the multislice approach. For tomograms with typical resolutions > 30 Å, the PA and WPOA are generally applicable. In single particle analysis, structures are being obtained up to 3.3 Å resolution [27] and are expected to improve further given advances in hardware developments such as direct electron detectors and phase plates. At those resolutions the PA and WPOA may be violated depending on the size of the macromolecule, whereas the TPGA again offers a good and fast alternative. The implementation of the exit wave simulations is freely available for non-commercial use upon request.

Acknowledgments

We acknowledge support from the FOM Industrial Partnership program No. 07.0599.

References

- [1] J. Frank, *Three-Dimensional Electron Microscopy of Macromolecular Assemblies: Visualization of Biological Molecules in Their Native State*, 2nd edition, Oxford University Press, 2006.
- [2] E.J. Kirkland, *Advanced Computing in Electron Microscopy*, 2nd edition, Springer Verlag, 2010.
- [3] M.M.J. Treacy, D.v. Dyck, A surprise in the first Born approximation for electron scattering, *Ultramicroscopy* 119 (2012) 57–62.
- [4] C.O.S. Sorzano, R. Marabini, J. Velázquez-Muriel, J. Bilbao-Castro, S.H.W. Scheres, J.M. Carazo, A. Pascual-Montano, XMIPP: a new generation of an open-source image processing package for electron microscopy, *Journal of Structural Biology* 148 (2004) 194–204.
- [5] M. van Heel, G. Harauz, E.V. Orlova, R. Schmidt, M. Schatz, A new generation of the IMAGIC image processing system, *Journal of Structural Biology* 116 (1996) 17–24.
- [6] T.R. Shaikh, H. Gao, W.T. Baxter, F.J. Asturias, N. Boisset, A. Leith, F. Frank, SPIDER image processing for single-particle reconstruction of biological macromolecules from electron micrographs, *Nature Protocols* 3 (2008) 1941–1974.
- [7] G. Tang, L. Peng, P.R. Baldwin, D.S. Mann, W. Jiang, I. Rees, S.J. Ludtke, EMAN2: an extensible image processing suite for electron microscopy, *Journal of Structural Biology* 157 (2007) 38–46.
- [8] S. Nickell, F. Förster, A. Linaroudis, W. Del Net, F. Beck, R. Hegerl, W. Baumeister, J.M. Plitzko, TOM software toolbox: acquisition and analysis for electron tomography, *Journal of Structural Biology* 149 (2005) 227–234.
- [9] H. Rullgård, L.-G. Öfverstedt, S. Masich, B. Daneholt, O. Öktem, Simulation of transmission electron microscope images of biological specimens, *Journal of Microscopy* 242 (2011) 234–256.
- [10] L. Reimer, H. Kohl, *Transmission Electron Microscopy*, Springer Series in Optical Sciences, 5th edition, vol. 36, Springer Verlag, 2008.
- [11] R.J. Hall, E. Nogales, R.M. Glaeser, Accurate modeling of single-particle cryo-EM images quantitates the benefits expected from using Zernike phase contrast, *Journal of Structural Biology* 174 (2011) 468–475.
- [12] M. Vulović, R.B.G. Ravelli, L.J. van Vliet, A.J. Koster, I. Lazić, H. Rullgård, O. Öktem, B. Rieger, Image formation modeling in cryo-electron microscopy, *Journal of Structural Biology* 183 (2013) 19–32.
- [13] J.M. Cowley, A.F. Moodie, The scattering of electrons by thin crystals, *Journal of the Physical Society of Japan, Supplement B* 17 (1962) 86–91.
- [14] J.C.H. Spence, *High-Resolution Electron Microscopy*, 3rd edition, Oxford University Press, 2003.
- [15] J.M. Gibson, Breakdown of the weak-phase object approximation in amorphous objects and measurement of high-resolution electron optical parameters, *Ultramicroscopy* 56 (1994) 26–31.
- [16] B.K. Jap, R.M. Glaeser, The scattering of high-energy electrons. II. Quantitative validity domains of the single-scattering approximations for organic crystals, *Acta Crystallographica A* 36 (1980) 57–67.
- [17] E.H. Linfoot, Transmission factors and optical design, *Journal of the Optical Society of America* 46 (1956) 740–747.
- [18] M. Vulović, *Modeling of Image Formation in Cryo-Electron Microscopy*, Ph.D. Thesis, Delft University of Technology, 2013.
- [19] L.-M. Peng, S.L. Dudarev, M.J. Whelan, *High-Energy Electron Diffraction and Microscopy*, Monographs on the Physics and Chemistry of Materials, vol. 61, Oxford University Press, 2004.
- [20] K. Ishizuka, N. Uyeda, A new theoretical and practical approach to the multislice method, *Acta Crystallographica A* 33 (1977) 740–749.
- [21] J.W. Goodman, *Introduction to Fourier Optics*, 3rd edition, Roberts and Company, 2005.
- [22] S. Goudsmith, J. Saunderson, Multiple scattering of electrons, *Physical Review* 57 (1940) 24–29.
- [23] L.M. Voortman, S. Stallinga, R.H.M. Schoenmakers, L.J. van Vliet, B. Rieger, A fast algorithm for computing and correcting the CTF for tilted, thick specimens in TEM, *Ultramicroscopy* 111 (2011) 1029–1036.
- [24] L.-M. Peng, G. Ren, S.L. Dudarev, M.J. Whelan, Robust parameterization of elastic and absorptive electron atomic scattering factors, *Acta Crystallographica A* 52 (1996) 257–276.
- [25] L.M. Voortman, E.M. Franken, L.J. van Vliet, B. Rieger, Fast, spatially varying CTF correction in TEM, *Ultramicroscopy* 118 (2012) 26–34.
- [26] A.I. Kirkland, S.L.-Y. Chang, J.L. Hutchison, Atomic resolution transmission electron microscopy, in: P.W. Hawkes, J.C.H. Spence (Eds.), *Science of Microscopy*, vol. 1, Springer, 2008, pp. 3–64.
- [27] X. Zhang, L. Jin, W.H. Fang, Q. Hui, Z.H. Zhou, 3.3 Å cryo-EM structure of a nonenveloped virus reveals a priming mechanism for cell entry, *Cell* 141 (2010) 472–482.